



Article

Identifying Deformation Drivers in Dam Segments Using Combined X- and C-Band PS Time Series

Jonas Ziemer ^{1,*}, Jannik Jänichen ¹, Gideon Stein ², Natascha Liedel ¹, Carolin Wicker ³, Katja Last ³, Joachim Denzler ², Christiane Schmullius ¹, Maha Shadaydeh ² and Clémence Dubois ⁴

- Department for Earth Observation, Friedrich Schiller University Jena, Leutragraben 1, 07743 Jena, Germany
- Computer Vision Group, Friedrich Schiller University Jena, Ernst-Abbe-Platz 2, 07743 Jena, Germany
- Department for Water Economy, Ruhrverband, Kronprinzenstraße 29, 45128 Essen, Germany
- German Aerospace Center, Institute of Data Science, Mälzerstraße 3, 07745 Jena, Germany
- * Correspondence: jonas.ziemer@uni-jena.de

Abstract

Dams play a vital role in securing water and electricity supplies for households and industry, and they contribute significantly to flood protection. Regular monitoring of dam deformations holds fundamental socio-economic and ecological importance. Traditionally, this has relied on time-consuming in situ techniques that offer either high spatial or temporal resolution. Persistent Scatterer Interferometry (PSI) addresses these limitations, enabling high-resolution monitoring in both domains. Sensors such as TerraSAR-X (TSX) and Sentinel-1 (S-1) have proven effective for deformation analysis with millimeter accuracy. Combining TSX and S-1 datasets enhances monitoring capabilities by leveraging the high spatial resolution of TSX with the broad coverage of S-1. This improves monitoring by increasing PS point density, reducing revisit intervals, and facilitating the detection of environmental deformation drivers. This study aims to investigate two objectives: first, we evaluate the benefits of a spatially and temporally densified PS time series derived from TSX and S-1 data for detecting radial deformations in individual dam segments. To support this, we developed the TSX2StaMPS toolbox, integrated into the updated snap2stamps workflow for generating single-master interferogram stacks using TSX data. Second, we identify deformation drivers using water level and temperature as exogenous variables. The five-year study period (2017–2022) was conducted on a gravity dam in North Rhine-Westphalia, Germany, which was divided into logically connected segments. The results were compared to in situ data obtained from pendulum measurements. Linear models demonstrated a fair agreement between the combined time series and the pendulum data $(R^2 = 0.5; MAE = 2.3 mm)$. Temperature was identified as the primary long-term driver of periodic deformations of the gravity dam. Following the filling of the reservoir, the variance in the PS data increased from 0.9 mm to 3.9 mm in RMSE, suggesting that water level changes are more responsible for short-term variations in the SAR signal. Upon full impoundment, the mean deformation amplitude decreased by approximately 1.7 mm toward the downstream side of the dam, which was attributed to the higher water pressure. The last five meters of water level rise resulted in higher feature importance due to interaction effects with temperature. The study concludes that integrating multiple PS datasets for dam monitoring is beneficial particularly for dams where few PS points can be identified using one sensor or where pendulum systems are not installed. Identifying the drivers of deformation is feasible and can be incorporated into existing monitoring frameworks.

Keywords: PSI; time series analysis; dam monitoring; segmentation; deformation drivers



Academic Editors: Antonio Miguel Ruiz Armenteros, Roberto Tomás, Joaquim João Sousa, M. Clara de Lacy and Zhenhong Li

Received: 20 June 2025 Revised: 18 July 2025 Accepted: 26 July 2025 Published: 29 July 2025

Citation: Ziemer, J.; Jänichen, J.; Stein, G.; Liedel, N.; Wicker, C.; Last, K.; Denzler, J.; Schmullius, C.; Shadaydeh, M.; Dubois, C. Identifying Deformation Drivers in Dam Segments Using Combined X- and C-Band PS Time Series. *Remote Sens.* 2025, 17, 2629. https://doi.org/10.3390/ rs17152629

Copyright: © 2025 by the authors. Licensee MDPI, Basel, Switzerland. This article is an open access article distributed under the terms and conditions of the Creative Commons Attribution (CC BY) license (https://creativecommons.org/licenses/by/4.0/).

Remote Sens. 2025, 17, 2629 2 of 22

1. Introduction

Dams fulfill various functions, including water supply, flood prevention, and energy generation. Furthermore, they play a crucial role in maintaining consistent water runoff throughout the year as well as offering recreational activities [1]. However, as civil structures, they have a potential risk of failure that, if poorly managed or neglected, can lead to severe societal, environmental, and economic damage. This underlines the importance of their continuous monitoring [2]. In Germany, the standards for dam monitoring are comparatively high [3,4]. Depending on the size of the dam, a comprehensive measuring setup is installed to monitor the deformation patterns over short and long-term periods. For concrete dams, the accuracy requirement for these in situ systems is reported with 5 mm [5]. The measurements are typically conducted with a pendulum system, enabling continuous monitoring, usually with one or more measurements per week. However, pendulum systems are not installed on every dam and only represent the deformations of a specific spot (e.g., the center of a dam), which may not coincide with other sections.

Technical advances in multi-temporal synthetic aperture radar interferometry (MT-InSAR) address these challenges by combining temporally dense time series with many observation points. MT-InSAR detects deformations by analyzing the phase differences of radar signals acquired over time. It relies on identifying Persistent Scatterers (PSs)—typically man-made structures or stable natural objects—that maintain a consistent backscatter across multiple SAR acquisitions. Using interferometric methods such as Persistent Scatterer Interferometry (PSI), deformations can be detected with millimeter precision. The technique assumes that deformation at each PS is temporally coherent, making it especially effective in urban areas. The number of Persistent Scatterers on a building is, apart from the material properties of the building, essentially dependent on the wavelength of the radar signal and the spatial resolution of the sensor. High-resolution X-band data, such as that from TerraSAR-X (TSX) (pixel footprint: 0.9×2.1 m), provide a high number of PS points on a local scale, making them ideal for dam monitoring. However, TSX data are not freely available and often lack consistent availability due to their high resolution. Additionally, the 11-day revisit cycle may be insufficient to meet the critical requirements for concrete dams with one or more deformation measurements per week. Freely available Sentinel-1 C-band data (S-1) provide sufficient PS measurements for most buildings and have been widely used for numerous analyses on a large scale [6–8]. Although a lower number of PS points is expected due to their lower spatial resolution compared to TSX (pixel footprint: 2.3×13.9 m) [9–11], the integration of S-1 data can greatly enhance monitoring capabilities by increasing both the spatial and temporal density of the time series when in combination with TSX data. This is particularly beneficial for monitoring not just the entire dam but also specific sections where anomalous deformation patterns could appear, underscoring the advantages of using different sensors [9]. This study uses data from TSX and S-1, to address two research objectives: first, to investigate the benefits of a combined PS time series instead of a single-sensor dataset for monitoring radial deformations in individual dam sections; and second, to leverage the increased density of the combined PS time series to analyze the influence of water level and temperature on the behavior of the SAR signal (i.e., the deformation of the dam).

1.1. Combining Different SAR Sensors for Dam Monitoring in Scientific Studies

MT-InSAR has been commonly used to monitor deformations of various types of dams, including earthfill dams [5,12–15], rockfill dams [16], and gravity dams [17–19]. A few studies have also focused on predicting the deformations of tailings dams using MT-InSAR to prevent failures [20,21]. Although X-band data, with their high resolution, suggest promising results for dam monitoring, numerous studies relied on C-band data

Remote Sens. 2025, 17, 2629 3 of 22

due to their free availability and extensive coverage [14–16,19,22]. Several studies have utilized MT-InSAR data from multiple sensors, as summarized in Table 1.

Milillo et al. [13] presented a multi-sensor cumulative deformation map for the Mosul earthfill dam in Iraq, incorporating 62 Cosmo SkyMed (CSK) X-band scenes and 32 S-1 scenes. Milillo et al. [18] fused 112 X-band acquisitions of different sensors (60 TSX, 52 CSK) in ascending mode to infer the deformation characteristics of an arch-gravity dam in Italy in spatial and temporal detail. However, the combination of datasets with different wavelengths for monitoring individual dam sections and evaluating the resulting time series with respect to their deformation drivers has not yet been thoroughly assessed. Since deformation patterns can vary across different parts of a dam, separating the object into logically defined segments allows for a more detailed analysis. This procedure has been successfully applied to other buildings, such as train stations [23].

1.2. Principles of Dam Deformation

Most dam wall reservoirs in Germany are impounded by a gravity dam (95%) [24]. Its cross-section is almost triangular, allowing the horizontal force of the water to be efficiently transferred into the bedrock through the self-weight of the dam [24]. Its deformation behavior is widely known and is illustrated in Figure 1. The water pressure, along with seasonal temperature effects, is primarily counteracted by the self-weight of the dam [25]. While the self-weight causes a deformation toward the upstream side, the water pressure leads to a tilt toward the downstream side with smaller deformations in the lateral areas compared to the middle [25]. Seasonal changes in temperature and water level result in periodic deformations on the crest that gradually decrease in the lower sections [25].

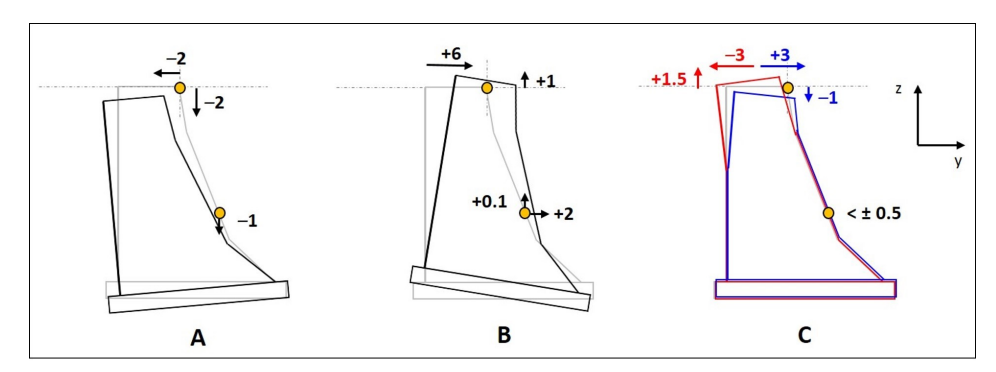


Figure 1. Deformations (in mm) calculated exemplary for two points in the middle of the Diemel gravity dam in Germany (height: 42 m; crest length: 194 m; reservoir capacity: 20 million m³). Predicted deformations are shown in horizontal (y) and vertical (z) direction, caused by the dam's self-weight (A), the water pressure at full impoundment (B), and temperature-induced displacements during summer (red) and winter (blue) (C). Negative horizontal values indicate a deformation to the upstream side, positive values a deformation to the downstream side (Adapted by Fleischer [25]).

Table 1. Selection of studies for monitoring dam deformations using multiple sensors for MT-InSAR.

Dam Type	Data	Study	
Earthfill Dam	TerraSAR-X, TanDEM-X	Lazecky et al., 2013 [12]	
Earthfill Dam	Sentinel-1, Cosmo SkyMed	Milillo et al., 2017 [13]	
Earthfill Dam	ERS-1/2, ENVISAT	Corsetti et al., 2018 [5]	
Earthfill Dam	ERS-1/2, ENVISAT, Sentinel-1	Ruiz-Armenteros et al., 2018 [14]	
Earthfill Dam	ERS-1/2, ENVISAT, Sentinel-1	Marchamalo-Sacristán et al., 2023 [15]	
Rockfill Dam	ERS-1/2, ENVISAT, Sentinel-1	Bayik et al., 2021 [22]	
Arch-Gravity Dam	TerraSAR-X, Cosmo-SkyMed	Milillo et al., 2016 [18]	

Remote Sens. 2025, 17, 2629 4 of 22

2. Study Site and Data

2.1. Study Site

The Glör Dam investigated in this study is located near Lüdenscheid in North Rhine-Westphalia, Germany, and is monitored by the Ruhrverband, a non-profit water management organization. The dam was built between 1903 and 1904 and serves to ensure the water release into the Glör River as well as for recreational purposes [26]. The arched gravity dam is 32 m high and 168 m long (Figure 2). Its downstream side is oriented toward the northeast (43°). The Glör Dam collects water from a catchment area of 7.2 km², creating a reservoir with a capacity of 1.95 million m³ [26]. It is equipped with several measurement techniques, such as pendulum and seepage water systems [26,27]. For extensive renovation, it was completely drained between November 2017 and January 2019, making it an ideal research object to investigate the effects on its deformation behavior during that time.

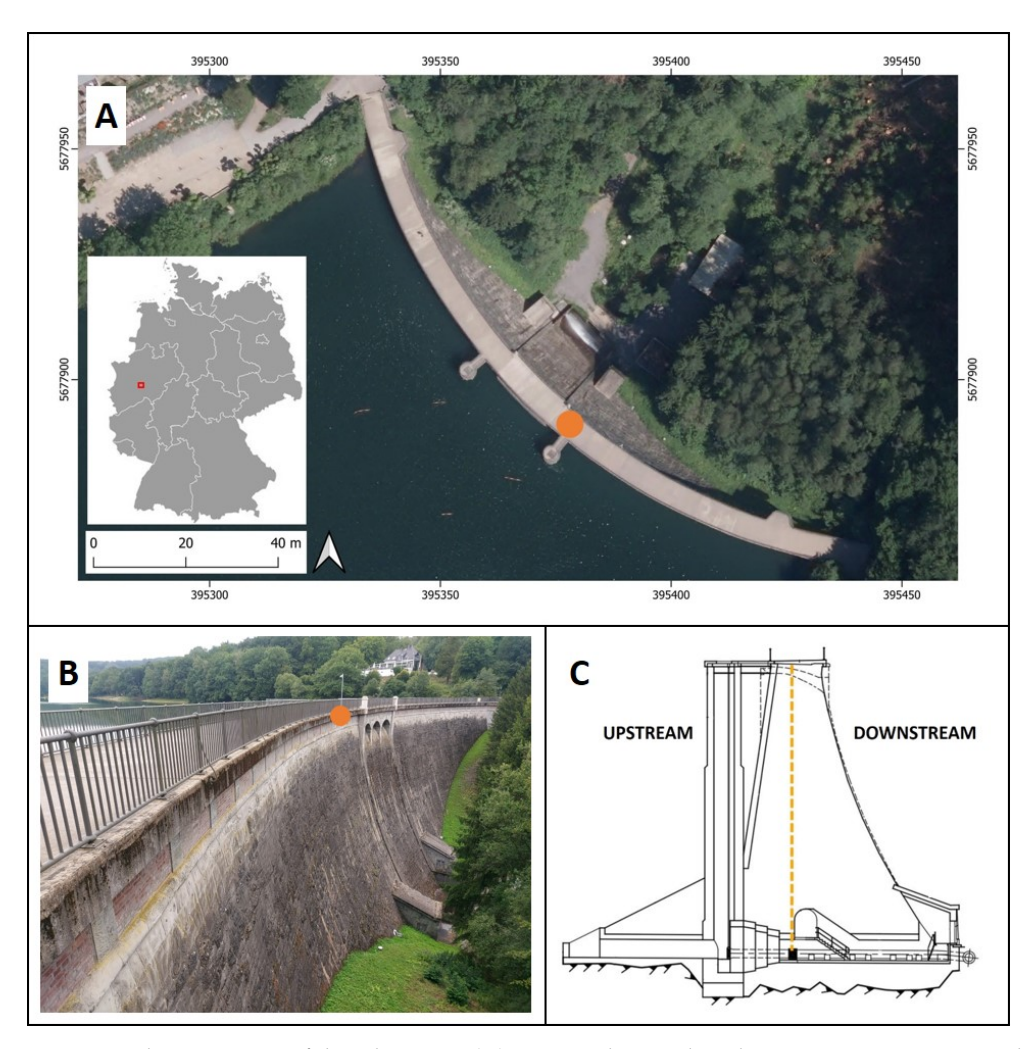


Figure 2. Characteristics of the Glör Dam: (**A**) Gravity dam with its location in Germany on a digital orthophoto. (**B**) Side view of the dam's downstream side. (**C**) Cross-section of the gravity dam [26,27]. The location of the pendulum system is marked in orange. Orthophoto: GDI-NRW [28], EPSG: 25832.

2.2. Data

This study covered a period of almost five years, spanning from November 2017 to August 2022. MT-InSAR time series from Sentinel-1 and TerraSAR-X were used in addition to in situ pendulum measurements, temperature, and water-level data.

Remote Sens. 2025, 17, 2629 5 of 22

2.2.1. Satellite Data and Digital Terrain Model

A total of 151 high-resolution TSX Stripmap (SM) scenes were utilized as the primary dataset. The time series was complemented by 145 Sentinel-1A C-band single-look complex (SLC) radar scenes acquired in Interferometric Wide Swath mode (IW) for the same observation period. Due to the dam's unfavorable alignment for radial deformations in the descending direction and the lack of TSX descending data, we only considered the ascending direction in this study. Table 2 lists the characteristics of the SAR data. Additionally, a digital terrain model (DTM) was utilized for PS processing. The DTM is freely provided in 1 m spatial resolution by the geodata infrastructure of the state of North Rhine-Westphalia (GDI-NRW) [28]. For DTM processing, the same methodology was applied as described in Jänichen et al. [19]: first, the DTM underwent a conversion to radar geometry, and second, it was employed in the preprocessing to achieve optimal coregistration of all SAR scenes. Due to computational load, the DTM was resampled to a spatial resolution of 5 m.

Table 2. Attributes of the SAR data used in this study [9].

	TerraSAR-X	Sentinel-1A	
Number of Scenes	151	145	
Pixel Footprint	$0.9 \times 2.1 \text{ m (ra} \times \text{az)}$	$2.3 \times 13.9 \text{ m (ra} \times \text{az)}$	
Temporal Resolution	11 days	12 days	
Acquisition Mode	Stripmap (SM)	Interferometric Wide Swath (IW	
Polarization	ΉĤ	VV	
Wavelength	X-band (\sim 3 cm)	C-band (\sim 5 cm)	
Relative Orbit Number	40	15	
Flight Direction	Ascending (351°)	Ascending (350°)	
Look Direction	81°	80°	
Incidence Angle	31.2°	38.9°	
Time Series Start Date	17 November 2017	19 November 2017	
Time Series End Date	21 August 2022	25 August 2022	
Reference Scene	7 May 2020	7 May 2020	

2.2.2. In Situ Data

To evaluate the validity of the PS deformation estimates, weekly pendulum data were provided by the Ruhrverband. Their precision is reported with 0.5 millimeters [29]. To identify the drivers of dam deformation, water level and temperature values were also provided by the Ruhrverband. The measurement sensors are directly located on the dam. A list of all available in situ data is shown in Table 3.

Table 3. In situ data used for the analysis with their corresponding measuring intervals [26,27].

Data	Temporal Resolution		
Pendulum Data (mm)	weekly		
Water Level (m)	daily		
Temperature (°C)	daily		

3. Methods

The methods applied in this study can be divided into four sections: (1) the PS analysis, (2) the segmentation of the dam, (3) the comparison of the combined PS time series with in situ pendulum data, and finally, (4) the identification of its deformation drivers. The general workflow is shown in Figure 3.

Remote Sens. 2025, 17, 2629 6 of 22

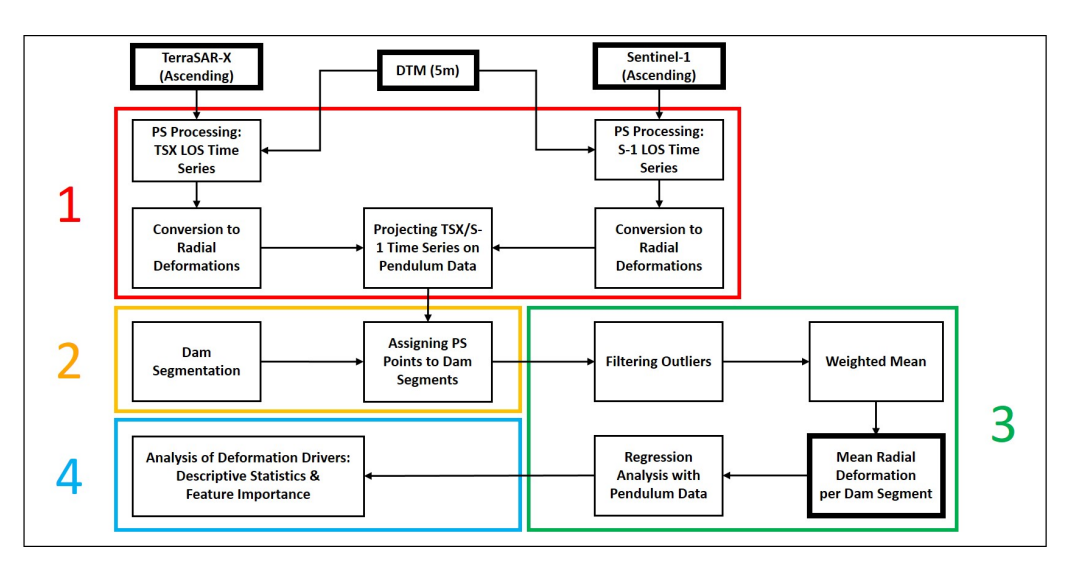


Figure 3. Workflow applied in this study: (1) PS analysis (red box). (2) Dam segmentation (orange box). (3) Comparison to pendulum data (green box). (4) Analysis of deformation drivers (cyan box).

3.1. Preprocessing and PS Analysis

Preprocessing was performed utilizing the open-source software package *snap2stamps*, which was specifically designed for the semi-automatic preprocessing of SAR SLC scenes. This includes subsetting, coregistration, interferogram generation, and the export of preprocessed data [30]. Since *snap2stamps* is only compatible with S-1 data, a new package called *TSX2StaMPS* was developed and implemented into a new version of *snap2stamps* [30,31]. It allows for the semi-automatic generation of single-master interferogram stacks using high-resolution TSX Stripmap data. A more detailed description of the workflow can be found on GitHub [30,31]. For PS analysis, *StaMPS* (*Stanford Method for Persistent Scatterers*) was utilized. We followed the same methodology as described in Grassi and Mancini [32]. Stable pixels were selected using the amplitude dispersion index [33] with a selection threshold of 0.4. The processing of TSX data was performed separately from the processing of S-1 data (see Figure 3).

The same date (7 May 2020) was selected as the reference scene in both stacks using SNAP's *InSAR Stack Overview* function. This also minimized errors caused by differing atmospheric conditions that could arise from using distinct reference scenes. The same set of reference points with high phase stability and no discernible deformation was selected. As no external leveling data were available, reference points were chosen using displacement data acquired by the German Ground Motion Service (BBD) [34], which was located close to the dams (<1.5 km). This approach aimed to ensure a high signal-to-noise ratio in the PS time series [35]. For coregistration and interferogram generation, a high-resolution external DTM (5 m) was utilized for both datasets to minimize DTM-induced errors within the processing chain.

The LOS time series of both sensors were converted into radial deformation values by considering the incidence angle and look direction of TSX and S-1 (see Table 2). Since deformations in LOS contain both vertical and horizontal displacement components, this metric could not be easily compared to pendulum data measured in the horizontal plane. The complete relationship between these components is illustrated in Equation (A1). The LOS values were converted to horizontal displacements, as the higher portion of motion on gravity dams is generally expected in the horizontal plane compared to the vertical component [25,36]. In this study, this assumption was confirmed by trigonometric measurements, which showed no significant vertical deformations over time [27]. The horizontal deformations (d_{hor}) were extracted by projecting the LOS deformations of both sensors onto

Remote Sens. 2025, 17, 2629 7 of 22

the horizontal plane. As a result, Equation (A1) simplifies to Equation (1) for TSX and Equation (2) for S-1:

$$d_{horTSX}[mm] = \frac{d_{TSX}}{\sin(\theta_{TSX})}$$
 (1)

$$d_{horS1}[\text{mm}] = \frac{d_{S1}}{\sin(\theta_{S1})} \tag{2}$$

where d_{TSX} and d_{S1} indicate the LOS deformation of TSX and S-1, and θ_{TSX} , θ_{S1} represent the incidence angle of the satellites. It is worth mentioning that this conversion is only possible if the displacements in one of the two dimensions are sufficiently small to be neglected. This procedure has been applied in several studies [8,18,36,37].

Due to the arched shape of the Glör Dam, both axes' orientations change for each PS point, and thus, the angle between the absolute north and the radial axis changes as well [19]. To convert the horizontal to radial deformations, we followed the same methodology as applied in Ziemer et al. [36]. These displacements can be directly compared to the pendulum measurements in the horizontal plane and are referred to as d_{rad} in the following. Equations (3) and (4) represent the conversion for TSX and S-1, respectively:

$$d_{radTSX}[mm] = \frac{d_{horTSX}}{\cos(\alpha_{rad} - \varphi_{TSX})}$$
 (3)

$$d_{radS1}[\text{mm}] = \frac{d_{horS1}}{\cos(\alpha_{\text{rad}} - \varphi_{\text{S1}})}$$
(4)

where α_{rad} is the radial angle of the corresponding PS point on the dam, and φ_{TSX} and φ_{S1} denote the look directions of TSX and S-1. Figure 4 illustrates all adaptations and the converted geometries of the PS datasets.

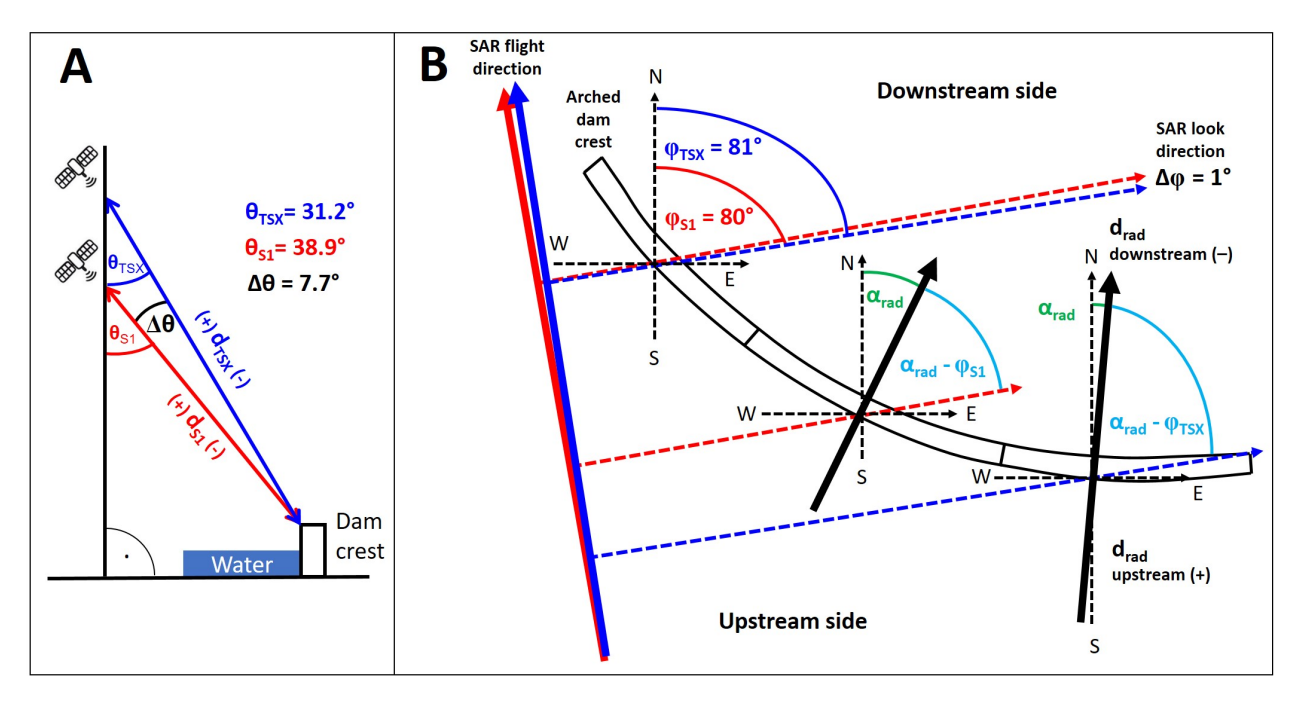


Figure 4. Illustration of the applied projections for TerraSAR-X (d_{TSX} , blue) and Sentinel-1 LOS geometry (d_{S1} , red) into radial deformation estimates: (**A**) Projection of the TSX and S-1 incidence angle (θ_{TSX} , θ_{S1}) onto the horizontal plane, applying Equations (1) and (2). (**B**) Projection of the TSX and S-1 look direction (ϕ_{TSX} , ϕ_{S1}) to convert horizontal deformations into radial values (d_{rad}), applying Equations (3) and (4). The difference between the sensors' look directions differs by only 1°.

Remote Sens. 2025, 17, 2629 8 of 22

3.2. Segmentation of the Dam

Due to the complex geometry of gravity dams, the precise location of PS points is generally difficult to determine—particularly when sensors with different spatial resolutions are used (see Table 2). To account for these potential variations due to inaccurate topographic height estimations, the Glör Dam was divided into segments by the Ruhrverband (Figure 5). Each segment was expected to exhibit distinct deformation behavior.

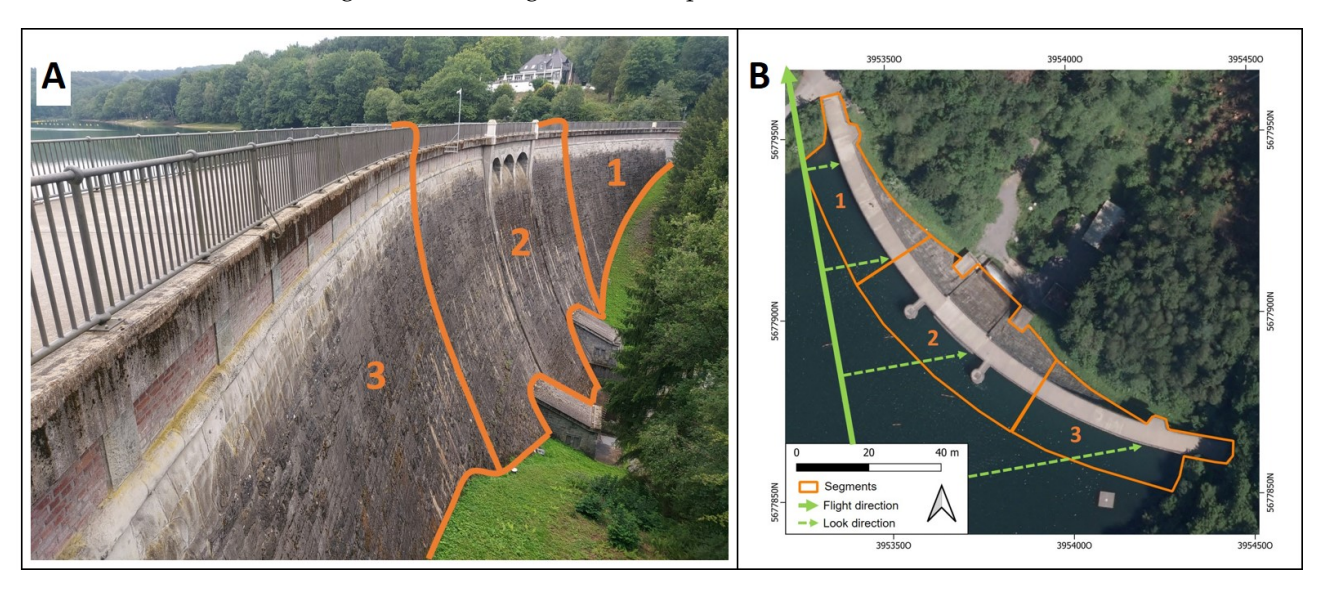


Figure 5. Segmentation (in orange) of the Glör Dam as viewed from the downstream side (**A**) and on a digital orthophoto (**B**). Segments 1–3 cover both sides of the dam. The ascending flight direction heads toward 350° and is shown in bold green. The dashed green lines indicate the look direction of the sensors (80°). Orthophoto: GDI-NRW [28], EPSG: 25832.

The segmentation allows assigning spatially close observation points with the same deformation profile to a segment and recognizing typical deformation patterns of the dam. The deformation of individual segments can be compared to other segments. A similar approach was tested by Schneider and Soergel [23] for buildings.

The Glör Dam was divided into three segments with similar widths (56 m)—one in the middle and two on the sides. Given the relatively small size of the dam, using three segments was sufficient, as a greater number would have resulted in an insufficient number of PS points per segment. For this reason, no subdivision into vertical segments was conducted. However, for larger dams (i.e., height > 50 m; crest length > 200 m), a more comprehensive segmentation into crest and toe segments may be appropriate. The segment boundaries on the upstream side of the crest were slightly shifted toward the water to account for sensor-specific differences in SAR geometry, which can approximately correspond to the size of the sensor's pixel footprint (see Table 2). Due to geometric distortions (i.e., layover and foreshortening) interacting with the water level of the reservoir and the dam wall (i.e., double-bounce effects) [18], maximum shifts of 10 m were expected.

3.3. Comparison of PS Deformation Time Series with In Situ Data

To compare the LOS deformations with the pendulum measurements, each PS point was assigned to a dam segment based on its 3D location. To generate a combined time series, the separately processed TSX and S-1 time series were calibrated against the pendulum data using linear regression. Specifically, individual regression models were fitted for both the TSX and S-1 time series with the pendulum data serving as the reference (Figure 6A). This approach aligned the respective slopes (i.e., representing the deformation trend) and intercepts of each satellite dataset with those of the pendulum measurements.

Remote Sens. 2025, 17, 2629 9 of 22

The calibration allowed both satellite time series—despite differing in acquisition dates and start times—to be projected onto the pendulum dataset, resulting in a harmonized, temporally densified TSX/S-1 time series (Figure 6B). Outlier values were excluded prior to fusion using a 1.5 interquartile range (IQR) filter applied to each dataset's distribution.

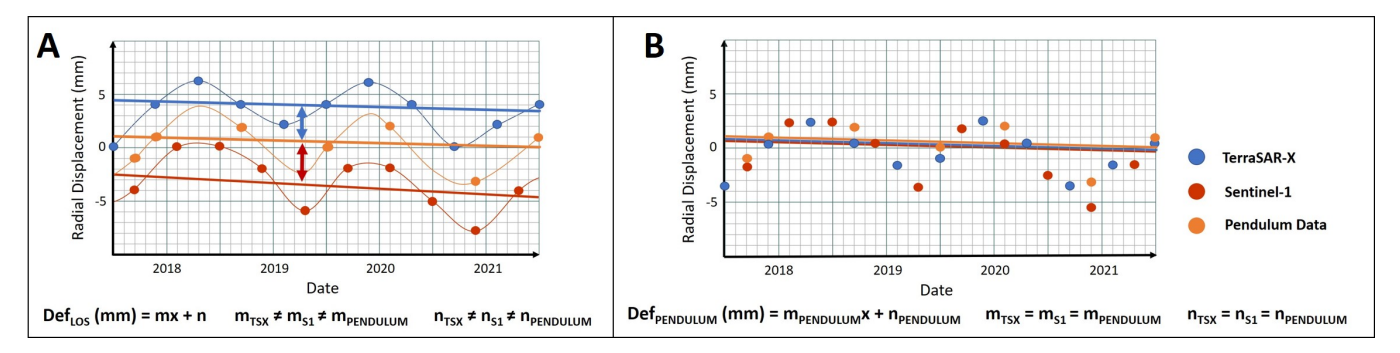


Figure 6. Calibrating the PS time series against the pendulum dataset: The TSX time series (blue) and the S-1 dataset (red) were calibrated against the pendulum dataset (orange) using linear regression models by aligning the slope (m) and intercept (n) of their respective regression models. **(A)** Time series before calibration with different regression slopes and intercepts. **(B)** Datasets after calibration with the same slope and intercept value as for the pendulum dataset.

To derive a spatially aggregated representation of dam deformation, we adopted a similar procedure to that applied by Schneider and Soergel [23], extending it to include two sensors. For a given segment *S*, the weighted mean deformation was calculated based on the number of available PS points from each sensor, as defined in Equation (5):

$$d_{mean}[mm] = \frac{(d_{radTSX} \cdot PS_{TSX}) + (d_{radS1} \cdot PS_{S1})}{PS_{total}}$$
(5)

where d_{radTSX} and d_{radS1} denote the mean radial deformation for TSX and S-1 in segment S, PS_{TSX} and PS_{S1} are the corresponding number of PS points in this segment, and PS_{total} is the sum of all PS points in segment S. The same procedure was applied to the single-sensor datasets of TSX and S-1.

Correlation analysis between PS and pendulum data was conducted utilizing descriptive statistics (R^2 , root mean square error (RMSE), mean absolute error (MAE)). To evaluate the dispersion of the PS data, we fitted a *LOESS* (*LOcally Estimated Scatterplot Smoothing*) regression [38] to determine the residual standard deviation. All linear models were checked for statistical significance (p < 0.01). Only acquisition dates available in both datasets, pendulum and PS data, were used. To assess the quality of the detected PS points, we calculated the temporal coherence of each PS point.

3.4. Water Level and Temperature-Induced Effects on the SAR Signal

To evaluate the effects of water level and temperature on the SAR signal, we divided the PS time series into three splits: drainage, reservoir filling, and full impoundment. First, we fitted a *LOESS* regression to each split and calculated the residual standard deviation of the deformation values around the *LOESS* curve. Second, we assessed the actual deviation of the PS deformation values from the pendulum data for each split using descriptive statistics (RMSE, MAE). Third, we analyzed the amplitude of deformation to identify potential long-term trends in the dam's behavior. Finally, we conducted a feature importance analysis on the PS data to gain deeper insights into which exogenous variables have the strongest effect on the behavior of the SAR signal. For this, we fitted individual linear regression models to the reservoir filling and full impoundment periods, and compared the feature usage via Shapley values [39]. To gain the most insightful results,

Remote Sens. 2025, 17, 2629

we not only tested the water level and the temperature of the current day as regressors but also considered lagged terms, interaction effects, and changes in water level and temperature from day to day. This relationship is described in Equation (6):

$$Y_{t} = \beta_{0} + \beta_{1}T_{t} + \beta_{2}W_{t} + \beta_{3}T_{t-1} + \beta_{4}W_{t-1} + \beta_{5}(T_{t} \cdot W_{t}) + \beta_{6}(T_{t-1} \cdot W_{t-1}) + \beta_{7}(T_{t} - T_{t-1}) + \beta_{8}(W_{t} - W_{t-1}) + \beta_{9}Tr_{t} + \varepsilon_{t}.$$

$$(6)$$

 T_t refers to temperature and W_t refers to the water level of the current day. T_{t-1} and W_{t-1} denote the lagged terms, representing past values of temperature and water level. The terms $W_t - W_{t-1}$, $T_t - T_{t-1}$ capture daily changes in water level and temperature, while $T_t \cdot W_t$ and $T_{t-1} \cdot W_{t-1}$ represent interaction effects between both variables, respectively. β_x represents model parameters, T_t denotes a linear trend, and ε_t indicates independent noise. All terms were individually normalized before model fitting. Importantly, the total model impact sums to one across all investigated variables. The model error is given as MAE.

4. Results

This section presents the results based on the two objectives outlined in Section 1: first, assessing the benefits of a combined TSX/S-1 time series, as compared to using data from a single sensor, for its suitability in dam monitoring by comparing it to pendulum data, and second, analyzing the drivers for dam deformation.

4.1. Suitability of Multi-Sensor PS Data for Gravity Dam Monitoring

A total of 28 PS points were detected on the Glör Dam: 19 by TSX and 9 by S-1. Two of the three segments benefited from the combination of both sensors. No S-1 PS points were found in Segment 3. Figure 7 illustrates the spatial distribution of PS points along the dam crest with many appearing shifted toward the upstream side and often located over water. This phenomenon will be discussed in Section 5. The coherence of each PS point ranged from 0.74 to 0.96, indicating generally high data quality. The temporal resolution for Segments 1 and 2 increased from 151 TSX scenes to 283 (+87%) utilizing the combined PS time series. This corresponds to an average temporal resolution of six days with a minimum time interval of one day and a maximum of 11 days.

Table 4 presents the statistics for the regression models between the PS time series and the pendulum data for each segment. The linear models between d_{mean} and the pendulum data exhibited significant p-values for all segments. Importantly, the mean amplitude in Segments 1 and 2 was higher for TSX than for S-1. In Segment 2, the differences between both sensors ranged between 3 and 4 mm. Accordingly, the standard deviation from the LOESS line was also greater for TSX.

Interestingly, the mean absolute error of the TSX data to the pendulum measurements was almost 1 mm larger than that of S-1. Given the high capabilities of TSX for infrastructure monitoring, this is an observation we would not necessarily have anticipated. Although a definitive explanation for this phenomenon is lacking, it appears that higher extreme values in the TSX deformation time series may be responsible for this observation. The time series of the single-sensor datasets are provided in Figure A1.

Figure 8 illustrates the mean radial deformation for the combined time series in all segments along with the pendulum data. During winter, characterized by low temperatures and higher water levels, the dam crest moved toward the downstream side (–). Conversely, in the summer months, with increasing temperatures and lower water levels, the deformations shifted toward the upstream side (+) [26,27].

Remote Sens. 2025, 17, 2629 11 of 22

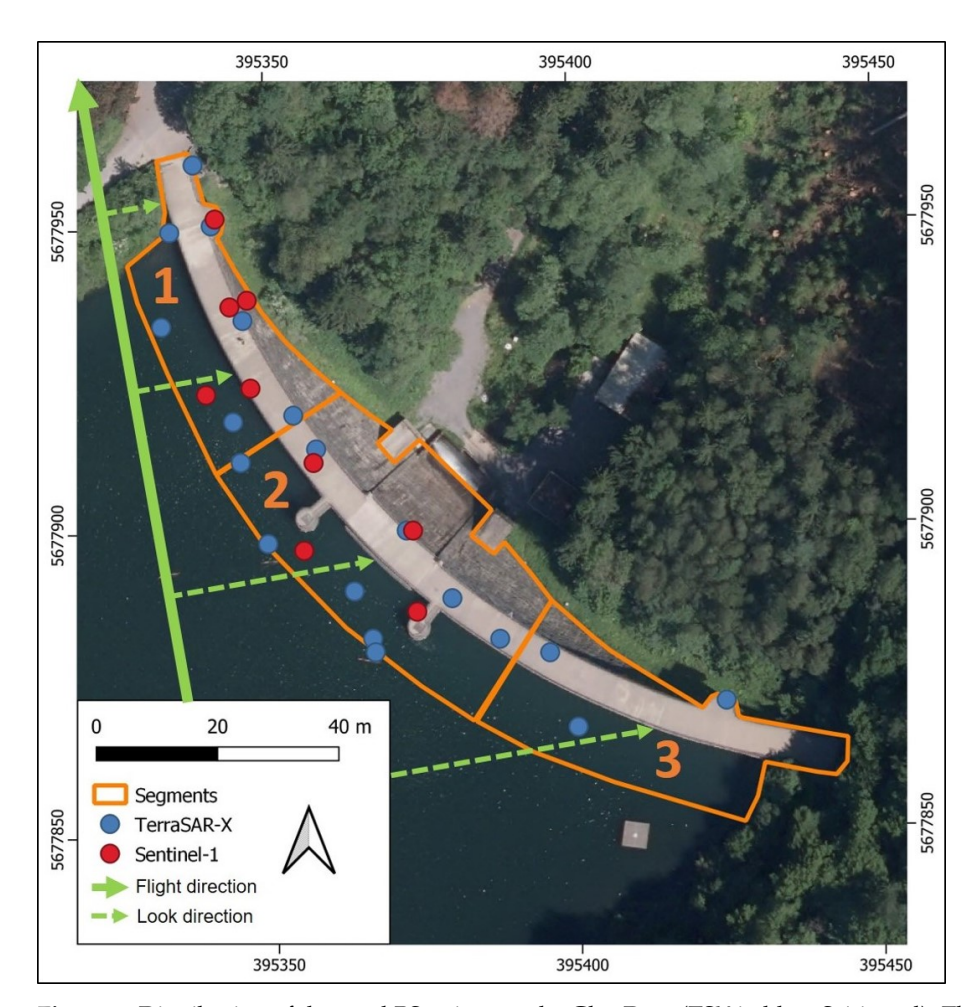


Figure 7. Distribution of detected PS points on the Glör Dam (TSX in blue; S-1 in red). The segments are shown in orange. The dashed green lines indicate the look direction of the sensors. Orthophoto: GDI-NRW [28], EPSG: 25832.

Table 4. Statistics for the regression models of d_{mean} and the pendulum data for each segment. Since no S-1 PS points were found in Segment 3, no models could be fitted. Amplitudes are shown as intervals in millimeters, ranging from minus (deformation to the downstream side) to plus (deformation to the upstream side). Due to the location of the pendulum system in the middle of the dam, a correlation analysis between PS time series and pendulum data was only conducted in Segment 2.

Sensor	Metric	Segment 1	Segment 2	Segment 3
TSX + S-1	Mean Amplitude (mm)	-7.8; +8.0	-13.2; +13.8	_
	R ² Pendulum	_	0.5	_
	MAE_{Pendulum} (mm)	_	2.3	_
	$SD_{\rm LOESS}$ (mm)	2.2	3.1	_
TerraSAR-X	Mean Amplitude (mm)	-7.8; +8.0	-13.2; +14.7	-13.1; +13.5
	R ² Pendulum	_	0.5	_
	MAE_{Pendulum} (mm)	_	2.7	_
	$SD_{\rm LOESS}$ (mm)	1.7	2.9	3.4
Sentinel-1	Mean Amplitude (mm)	-6.9; +7.1	-10.5; +10.0	_
	R ² _{Pendulum}	_	0.6	_
	MAE_{Pendulum} (mm)	_	1.9	_
	$SD_{\rm LOESS}$ (mm)	2.2	2.6	_

In the middle segment of the Glör Dam, d_{mean} amplitudes ranged from -13.2 mm to +13.8 mm for the combined PS time series, demonstrating a mean absolute error of 2.3 mm to the pendulum data (see Table 4). The standard deviation to the *LOESS* line

Remote Sens. 2025, 17, 2629 12 of 22

ranged between 2.6 mm and 3.1 mm in the middle segment. Linear models fitted with the pendulum data revealed moderate R^2 for both sensors (0.5 $\leq R^2 \leq$ 0.6). The fact that the S-1 time series indicated a higher correlation and lower errors with the pendulum data than that from TSX is noteworthy, since TSX data are known for their capability to precisely monitor the deformations of individual infrastructures.

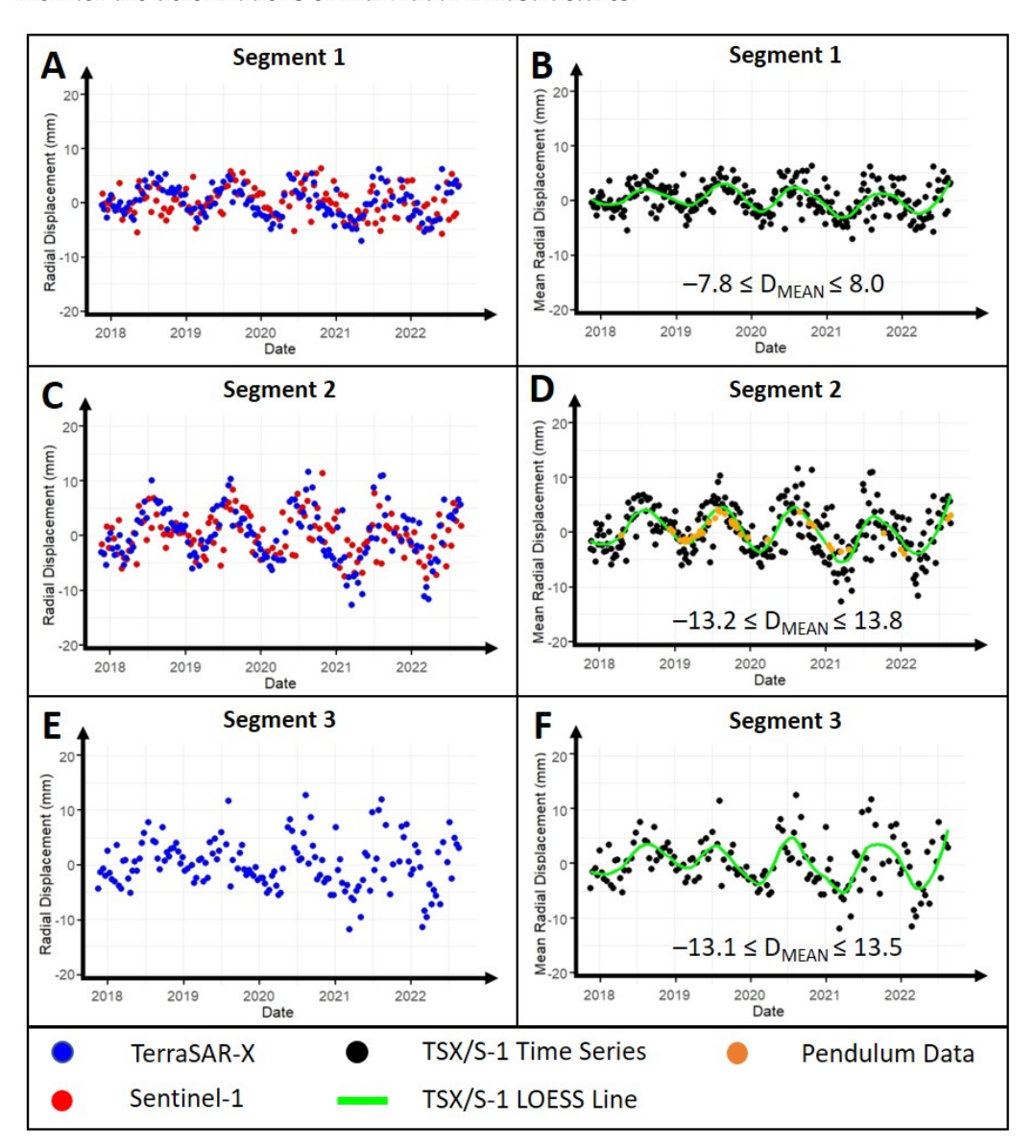


Figure 8. Mean radial deformation (d_{mean}) for all segments of the Glör Dam divided by SAR sensor (**left**) and fitted with a *LOESS* regression (**right**). (**A**,**B**) Western Segment 1. (**C**,**D**) Middle Segment 2. (**E**,**F**) Eastern Segment 3, which only consists of TSX PS points. Due to the location of the pendulum system at the center of the dam, PS time series were compared to pendulum data only in Segment 2 (orange). The radial deformation amplitude is given as an interval in millimeters.

The mean deformation signals of Segments 1 and 3 exhibited the same seasonal pattern as in Segment 2 but with lower deformation amplitudes. In the combined time series of Segment 1, amplitudes ranged between -7.8 mm and +8 mm. On the one hand, the lower amplitude compared to Segment 2 is induced by the dam's design, since the highest amount of deformation typically occurs in the center of a gravity dam [18,25]. However, as can be seen in Figure 8, considerable differences occurred between the two side segments, where Segment 3 almost reached the same deformation amplitude as evident in Segment 2. Compared to the LOS deformations in Figure A2, this difference can be attributed to the

Remote Sens. 2025, 17, 2629 13 of 22

lower sensitivity to radial deformations of Segment 3 [36]. This phenomenon will be explicitly discussed in Section 5.

4.2. Assessing the Influence of Water Level and Temperature on the SAR Signal

The dam exhibits seasonal deformation patterns primarily induced by water level fluctuations and seasonal temperature changes (i.e., thermal expansion) [25]. As shown in Figure 9, a similar seasonal pattern was evident between the temperature data and the SAR signal. Notably, the Glör Dam was fully drained from November 2017 to January 2019, eliminating water pressure as a contributing factor to deformation during that period.

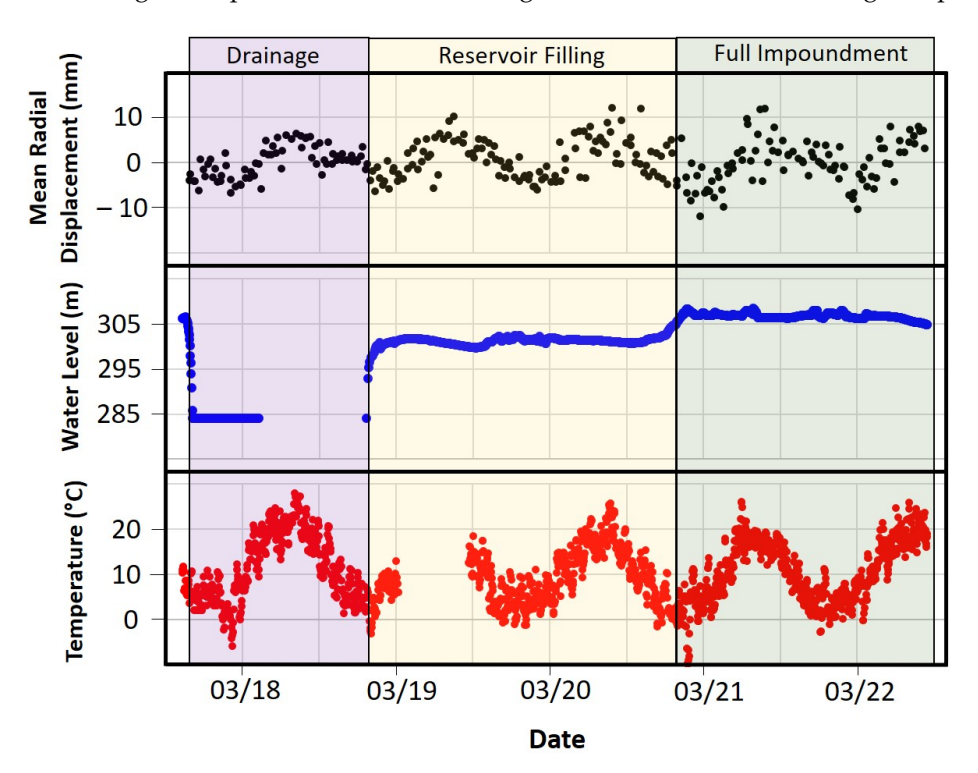


Figure 9. d_{mean} (in mm) in Segment 2 of the Glör Dam, shown alongside the corresponding water levels (in m) and temperatures (in °C) during the three phases drainage (purple), reservoir filling (yellow), and full impoundment (green). Due to the renovation of the Glör Dam, the measuring setup was also updated, resulting in data gaps in both water level and temperature records.

However, the drainage did not appear to significantly impact the periodic deformation pattern observed in the PS time series, suggesting that temperature was the sole driver of deformation during this time.

Interesting patterns in the behavior of the SAR signal were observed during the reservoir filling and the first full impoundment following the renovation of the dam (Figure 10). While the RMSE and MAE for the pendulum data remained below 1 mm during the drainage phase, these errors increased during reservoir filling to 2.9 mm (RMSE) and 2.4 mm (MAE), reaching their maximum during full impoundment with 3.9 mm (RMSE) and 2.7 mm (MAE) (Figure 10A). The standard deviation from the *LOESS* regression was also minimal during drainage (1.8 mm), rose to 2.9 mm during reservoir filling, and peaked during full impoundment, exceeding 3 mm. This trend is also evident in the residuals of the *LOESS* regression (Figure 10C), which show increasing variance around the *LOESS* line from drainage to full impoundment.

Regarding the amplitude of the SAR signal, considerable differences were observed among the three splits (Figure 10B). While the drainage phase was characterized by a relatively small amplitude range ($-5.9 \text{ mm} \le 1.5 \text{ IQR} \le +6.9 \text{ mm}$), it increased during reservoir

Remote Sens. 2025, 17, 2629 14 of 22

filling, reaching a range of nearly 20 mm, and peaked during full impoundment with values ranging from -12.6 mm to +11.1 mm. Interestingly, the mean deformation values remained consistent during the transition from drainage to reservoir filling ($d_{mean} = 0.7$ mm), but they decreased to -1 mm during full impoundment. This suggests that the final five meters of water level rise had a notable impact on deformation, displacing the dam crest approximately 1.7 mm toward the downstream side due to increased water pressure.

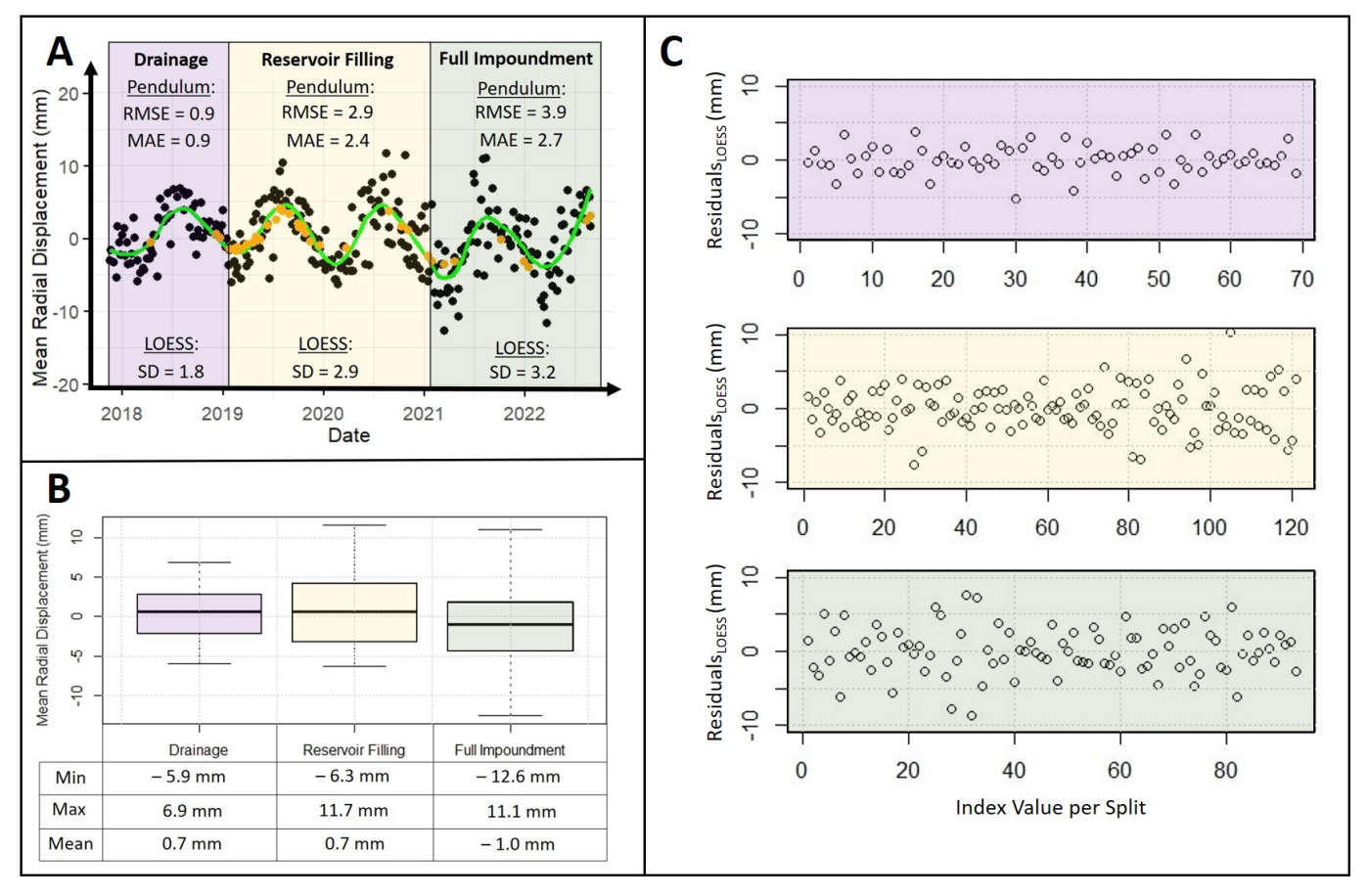


Figure 10. Evaluating the effect of water level and temperature on the PS time series in the three phases: drainage (purple), reservoir filling (yellow), and full impoundment (green). (**A**) Mean radial deformation (in mm) in the middle Segment 2 of the Glör Dam shown with the pendulum data (orange) and the fitted *LOESS* line (green). The RMSE and MAE between the PS time series and the pendulum data are given in mm for each split. The standard deviation of the *LOESS* regression is also given in mm. (**B**) Distribution of PS deformation amplitudes displayed as a boxplot with the minimum, maximum, and mean value per split. (**C**) Distribution of PS time series residuals to the fitted *LOESS* regression (in mm). The index value corresponds to the number of samples (i.e., acquisition dates) per split.

The analysis of the feature importance confirmed the temperature as the variable with the highest impact on the model output. As shown in Figure 11, the summed model impact for the two temperature values (T_t , T_{t-1}) was 0.71 during reservoir filling and 0.73 during full impoundment. While general dynamics changed between reservoir filling and full impoundment, the feature importance of the water level increased for full impoundment. Notably, however, this effect seems to primarily come in an indirect form through the interaction with the temperature values (interaction terms), suggesting multiplicative effects. This is consistent with the intuition that the signal variance was highest for the full impoundment, as it is more driven by the water level. We assume that the increased importance of the trend parameter can be attributed to the fact that the seasonal coverage changed between the two splits. Finally, it is worth mentioning that the predictive power

Remote Sens. 2025, 17, 2629 15 of 22

of the regression model during full impoundment was higher (measured by lower mean absolute residuals: 0.128 during full impoundment and 0.132 during reservoir filling). This again suggests that the effects of lower water levels were either diminished or highly nonlinear, and that the final meters of reservoir filling had the greatest direct impact on dam deformation, as measured by the PS time series.

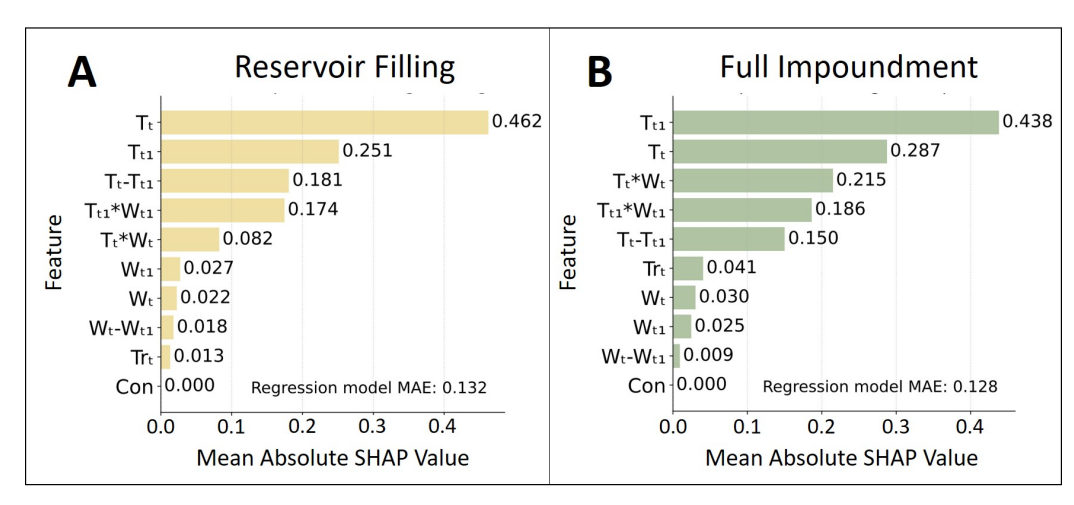


Figure 11. Mean absolute Shap values during reservoir filling (**A**) and full impoundment (**B**). The sum of all variables on the model impact is 1. Notably, the importance of *W* increases through interaction effects during full impoundment.

5. Discussion

This study examined the benefits of combining PS datasets from different wavelengths for dam monitoring and investigating the impact of exogenous variables on the behavior of the SAR signal. In this section, the results are discussed with respect to the objectives presented in Section 1.

5.1. Combining PS Datasets for Dam Monitoring: A Benefit for Dam Operators?

This study investigated the potential of combining PS datasets of multiple SAR sensors for dam monitoring. Major advantages were observed compared to using single-sensor datasets, which was consistent with findings from other studies [9–11]. These benefits include the spatial and temporal densification of the time series and the aggregation of individual PS points into segments with varying deformation profiles, underscoring their utility in dam monitoring. Integrating freely available S-1 data with high-resolution TSX data could enhance spatial and temporal coverage in individual dam segments. TSX proved particularly valuable in segments where S-1 failed to detect PS points, thereby enhancing deformation monitoring.

Utilizing both sensors reduced the observation interval from 11 to 6 days in two of the three segments. Although TSX is widely known for its huge capabilities in infrastructure monitoring [12,18], the fact that the PS time series acquired by S-1 indicated a lower signal variance and slightly higher correlations with the pendulum data positions Sentinel-1 as a powerful alternative for PS-based dam monitoring. This is even more evident in the fact that TSX data are not freely available and often lack availability for many sites. Existing ground motion services (e.g., BBD, European Ground Motion Service) also provide analysis-ready S-1 PS time series for comparison. If individual dams or segments are not adequately covered by S-1, or if critical deformation patterns are detected that require further investigation, S-1 data could be supplemented locally with high-resolution X-band data or in situ campaigns.

Remote Sens. 2025, 17, 2629 16 of 22

The study revealed very similar deformation patterns between the PS time series and the pendulum measurements. The dam exhibited seasonal deformations linked to changes in water level and temperature, which were visible in both PS datasets. The MAE of the combined PS time series to the pendulum data (2.3 mm) indicated that the PSI technique may not be precise enough to replace pendulum measurements, whose precision is reported with 0.5 mm [29]. However, the error is far below the accuracy requirement of 5 mm proposed by Corsetti et al. [5] for concrete dams. Compared to trigonometric measurements, reported with 3 mm precision [29], the PSI technique also yields lower uncertainties and considerably reduced revisit times, making it a valuable tool for dam monitoring when pendulum data are unavailable. On the Glör Dam, this is particularly relevant for the side segments, which lack dedicated pendulum systems. As a result, PS-based deformations in these segments could not be compared to in situ data.

5.2. Water Level and Temperature—The Main Drivers for Deformation?

The temperature was confirmed as the main driver for seasonal deformations of the dam wall. This aligns with the widely known thermal expansion patterns of buildings observed in other studies [10]. However, the fact that the periodic deformation seems completely independent of the water level in the reservoir is noteworthy. The analysis demonstrated an increase in signal variance with reservoir filling, suggesting that the water level affects the short-term variance, while temperature seems more responsible for the long-term trend deformation. Notably, this interpretation is also consistent with the feature importance that was performed. During full impoundment, despite the signal having a higher variance, the predictability of the signal (measured here by model MAE) was not reduced. Further, as the effect of water level in the model generally increased during this period, the additional variance in the signal is likely explainable by an increased impact of water level on dam deformation.

Future observations of full or partial drainage events present a valuable opportunity to further substantiate this hypothesis. Such data will be instrumental in developing more sophisticated statistical models beyond linear regression, thereby enabling a precise characterization of the functional relationships between dam deformation and exogenous drivers. A deeper understanding of the underlying mechanisms, in combination with more sophisticated models, could, for instance, be leveraged to accurately predict dam deformations, as was shown in recent studies [36]. Incorporating more exogenous variables, such as frost and groundwater levels, could additionally contribute to a more comprehensive analysis of deformation drivers.

5.3. Challenges of the Proposed Methodology

The PSI technique has proven to be an effective tool for observing dam deformations provided that certain requirements are met. These include the availability of data within the study area as well as favorable topographic conditions. For deformation interpretation, the alignment of the dam to the look direction of the satellite sensor emerges as one of the most essential criteria for comparability to in situ measurements [36]. Due to the satellites' flight direction, the PSI technique accurately retrieves radial deformations occurring in the east/west direction. The flight paths of both sensors are oriented to the northwest, but the look direction heads toward east–northeast (80°), since it is perpendicular to the flight direction (see Figure 5B). Consequently, the optimal orientation with the highest sensitivity to radial deformations is parallel to the flight track [10]. Particularly in Segment 3, radial deformations appear almost perpendicular to the look direction of the sensors. The fact that radial deformations in Segment 3 are significantly larger than those in Segment 1 is not evident in the LOS data (see Figure A2). Consequently, projecting the LOS signal into

Remote Sens. 2025, 17, 2629 17 of 22

the radial axis would result in substantial errors when compared to the pendulum data and may not accurately reflect the true amplitude of deformation in these segments. It can be generally assumed that the greater the angle between φ_{TSX} or φ_{S1} and α_{rad} , the smaller the PS sensitivity to radial deformations [36]. Therefore, not all PS points or dam segments may be equally suited for a PS-based monitoring strategy with multiple SAR sensors. This may require filtering adequate PS points during post-processing to avoid misinterpreting deformation estimates.

It is important to mention that converting LOS to radial PS deformations can only be carried out on dams that demonstrably do not experience significant vertical movements [36]. Unlike embankment dams, vertical deformations on gravity dams are generally lower as they are founded on solid rock formations [40]. Consequently, the LOS signal could be converted to horizontal (i.e., radial) deformations by neglecting the vertical component [18,36]. This approach may not apply to other types of dams and is highly case-specific.

Both PS datasets exhibit comparable seasonal amplitudes of approximately ±13 mm in the middle segment (see Figure 8), indicating consistency between TSX and S-1 data. Differences in signal variance could be caused by variations in time series length, the number of processed images, the quality of reference scenes, the PS network quality in individual stacks, and the position of the AOI in the range direction. However, the fact that the S-1 time series showed lower variances and higher correlation with the pendulum data in the middle segment compared to TSX is remarkable. Importantly, the disparity in pixel size between TSX and S-1 does not translate into a substantial difference in the number of PS points on the dam. The comparison between both sensors revealed that TSX detected approximately twice as many PS points as S-1. Given that TSX has a pixel size 17 times smaller than S-1 (see Table 1), one may expect a proportional increase in PS points. However, this does not hold true for the Glör Dam. TSX detects relatively fewer stable scatterers than S-1, indicating that pixel size alone cannot account for the variation in PS points on the dam. Differences in wavelength also influence how stable scatterers interact with each sensor. This phenomenon relates to the radar backscattering intensity, which depends on the ratio of scatterer size to radar wavelength [41]. The dam crest, along with its railing and water outlets, may predominantly feature larger scatterers, resulting in TSX detecting only twice as many PS points as S-1. Importantly, this ratio varies from dam to dam and essentially depends on the material properties and the number of detected PS features.

A major challenge of this study was handling the PS analysis of two sensors with differing spatial resolutions. While one possible approach would have been to downsample the TSX data to match the resolution of S-1 for direct comparability, we chose instead to retain the full resolution of TSX to maximize the number and spatial density of PS points. Due to the complex geometry of the Glör Dam, many of these points tend to shift toward the upstream side. It is important to note that accurately determining the precise locations of PS points is often challenging. To minimize errors induced during coregistration, a highresolution DTM was utilized. In this case, inaccuracies in position are not primarily caused by errors in geocoding. The vertical walls of gravity dams result in foreshortening and layover at the top of the crest. Interactions with the water surface lead to double-bounce effects on the dam crest [18]. As a result, the position of the scatterer is referenced to the image pixel corresponding to its runtime. As both sensors are right-looking systems operated in ascending mode, some points are slightly shifted toward the sensor [42]. Due to the spatial resolution of the sensors, the pixel position also varies by this order of magnitude, leading to PS points located several meters away from the dam. To overcome this limitation, segments were defined with a tolerance of 10 m to the upstream side to account for double-bounce effects caused by seasonal fluctuations in water level. The size of the segments was chosen to minimize uncertainty during topographic phase removal

Remote Sens. 2025, 17, 2629 18 of 22

due to the dam's complex geometry and the different spatial resolutions of the sensors. Since the number of PS points detected on the Glör Dam was relatively low, the points were aggregated into a mean deformation profile, which was calculated as the weighted mean of all points within each segment. This approach not only enabled conclusions to be drawn about deformation behavior in different areas of the dam but also minimized the influence of lower-quality PS points, such as those with low signal-to-noise ratios or outliers in the deformation time series.

6. Conclusions

This study introduced a spaceborne multi-sensor approach for monitoring a gravity dam in Germany using PS datasets from different wavelengths. Applying TSX2StaMPS as part of the updated *snap2stamps* package, the S-1 data were integrated with high-resolution TSX data to enhance the spatial and temporal resolution of the time series. The study yielded promising results for monitoring individual dam segments, revealing fair agreement with the pendulum data in the center of the investigated dam ($R^2 = 0.5$; $MAE_{Pendulum} = 2.3$ mm). By incorporating S-1 data with high-resolution TSX data, spatial and temporal monitoring could be enhanced in two of three segments, doubling the number of analyzed SAR scenes and increasing the number of PS points on the dam. The proposed approach proved particularly valuable in segments where one of the sensors failed to detect PS points, enabling a comprehensive observation of all dam sections. The sensitivity of PS points to radial deformations evolved as one of the most essential criteria for deformation interpretation. An optimal alignment of the dam crest to the look direction of the satellite sensor is crucial to ensure comparability to in situ radial measurements acquired by pendulum systems. Therefore, not all dams or dam sections may be equally suited for a PS-based monitoring strategy with multiple SAR sensors.

The temperature was identified as the long-term component for periodic deformations of the gravity dam. The drainage of the Glör Dam indicated that these deformation patterns are completely independent of water level, and thus, the thermal expansion of the dam could be made responsible for the total deformation during this period. With the reservoir filling after renovation, the variance in the PS time series increased from 0.9 to 3.9 mm in RMSE, indicating that the water level is more responsible for short-term variations in the SAR signal. With the full impoundment of the reservoir, the mean amplitude of deformation decreased about 1.7 mm toward the downstream side of the dam as a result of the higher water pressure. The last five meters of water level rise resulted in higher feature importance due to interaction effects with temperature.

Future research could concentrate on causal analyses between the deformation of the dam and its influencing factors to obtain a deeper insight into the physical understanding and mechanisms of dam movement. As temperature was identified as the primary long-term driver of deformation, structural trends and changes to the dam could also be analyzed with regard to climate change.

Author Contributions: Conceptualization, J.Z., K.L., G.S. and C.D.; methodology, J.Z., J.J., G.S., N.L., K.L. and C.D.; validation, J.Z. and G.S.; formal analysis, J.Z.; investigation, J.Z. and G.S.; resources, C.W. and K.L.; software, J.Z. and C.D.; data curation, J.Z. and G.S.; writing—original draft preparation, J.Z. and G.S.; writing—review and editing, C.D., J.J., N.L. and C.W.; visualization, J.Z. and G.S.; supervision, C.D., K.L., J.D., M.S. and C.S.; project administration, C.D., J.Z. and C.S.; funding acquisition, C.S. All authors have read and agreed to the published version of the manuscript.

Funding: This research received external funding provided by the Federal Ministry for Economic Affairs and Climate Action (BMWK) due to an enactment of the German Bundestag under Grant No. 50EE2202A.

Remote Sens. 2025, 17, 2629

Data Availability Statement: The raw data supporting the conclusions of this article will be made available by the authors on request.

Acknowledgments: We acknowledge financial support through DLR with funds provided by the Federal Ministry for Economic Affairs and Climate Action (BMWK) due to an enactment of the German Bundestag under Grant No. 50EE2202A. We want to thank DLR for providing high-resolution TerraSAR-X Stripmap data and CloudFerro for their support using the EO-lab cloud platform. We would also like to thank the Freizeitschwerpunkt Glörtalsperre GmbH for permission to publish this study.

Conflicts of Interest: The authors Carolin Wicker and Katja Last are employed by the Department for Water Economy, Ruhrverband. The remaining authors declare that the research was conducted in the absence of any commercial or financial relationships that could be construed as a potential conflict of interest. The funders had no role in the design of the study; in the collection, analyses, or interpretation of data; in the writing of the manuscript; or in the decision to publish the results.

Appendix A

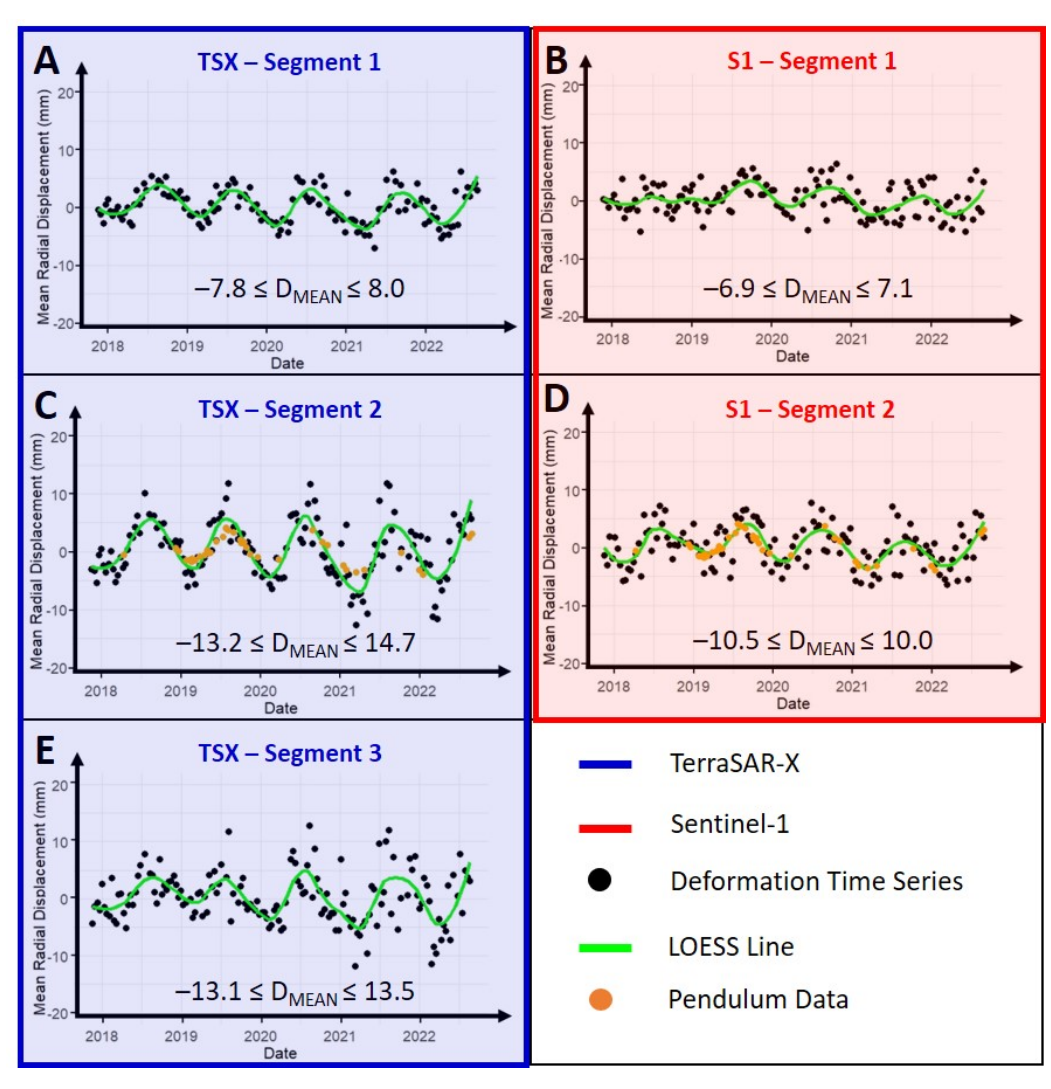


Figure A1. Single-sensor time series of TSX (**A**,**C**,**E**, blue) and S-1 (**B**,**D**, red) shown as d_{mean} for all segments of the Glör Dam. The trend curves of Segment 2 were fitted using a *LOESS* regression (green). Due to the location of the pendulum system at the center of the dam, PS time series were compared to pendulum data only in Segment 2 (orange). The radial deformation amplitude is given as an interval in millimeters.

Remote Sens. 2025, 17, 2629 20 of 22

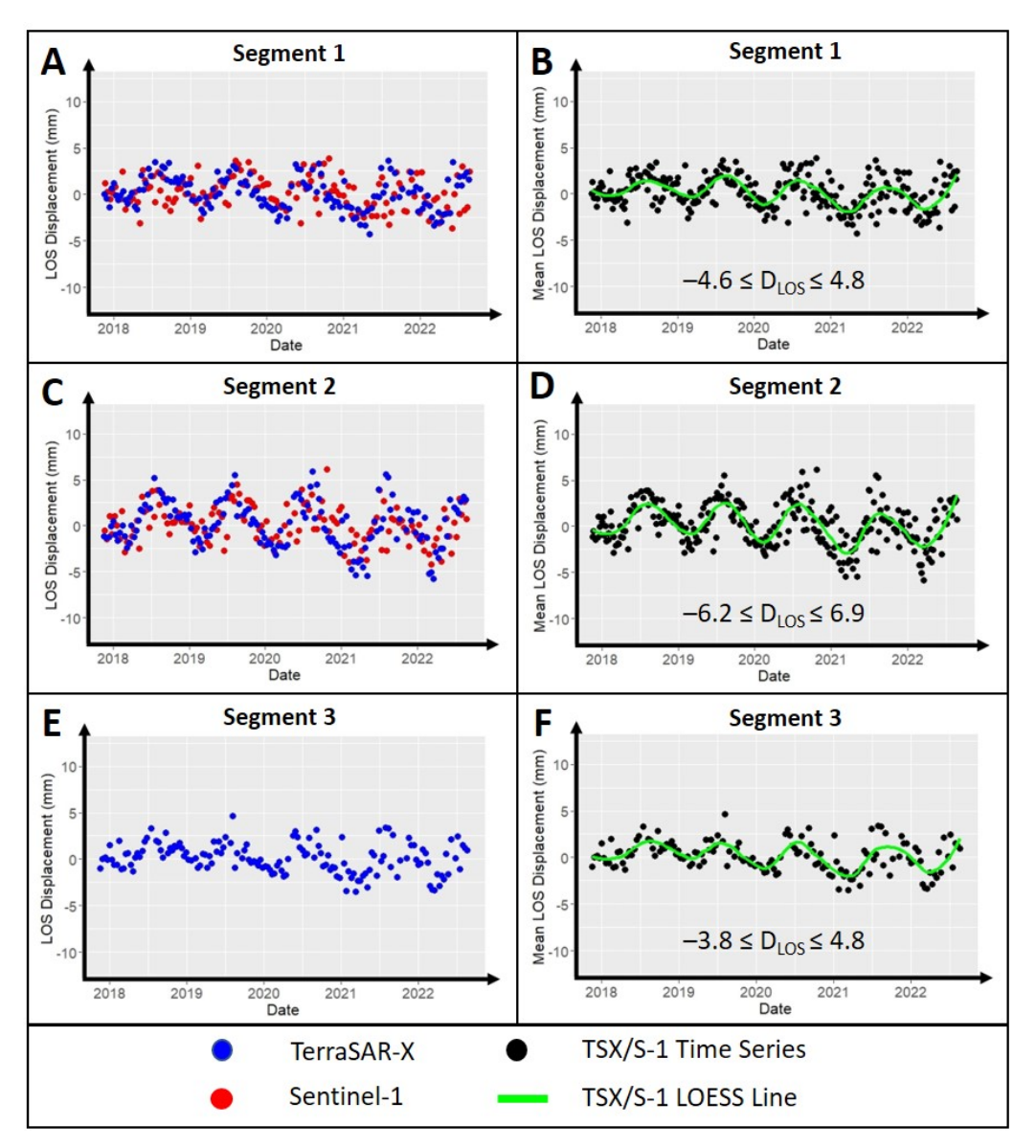


Figure A2. Mean LOS deformation for all segments of the Glör Dam divided by the SAR sensor (**left**) and fitted with a *LOESS* regression (**right**). (**A,B**) Western Segment 1. (**C,D**) Middle Segment 2. (**E,F**) Eastern Segment 3, which only consists of TSX PS points. Due to the different acquisition geometries between SAR data and pendulum data, the LOS time series could not be compared to radial pendulum data. The LOS deformation amplitude is given as an interval in millimeters.

Appendix B

A conversion from a single LOS direction (d_{LOS}) to a displacement d, corresponding to the expected direction of the detected movement, is performed as follows [43,44]:

$$d[\text{mm}] = \frac{d_{LOS}}{\cos(\alpha_V) \cdot \cos(\theta_S) + \sin(\alpha_V) \cdot \cos(\alpha_{\text{rad}} - \varphi_S) \cdot \sin(\theta_S)}$$
(A1)

where $\theta_{\rm S}$ represents the incidence angle of the sensor, and α_V denotes the angle between the vertical direction and the true deformation direction. The angular difference between the true north radial angle of a detected scatterer ($\alpha_{\rm rad}$) and the sensor's look direction ($\phi_{\rm S}$) ranges between 0° and 90°.

Remote Sens. 2025, 17, 2629 21 of 22

References

- 1. Baxter, R. Environmental effects of dams and impoundments. Annu. Rev. Ecol. Syst. 1977, 8, 255–283. [CrossRef]
- 2. de Paiva, C.A.; da Fonseca Santiago, A.; do Prado Filho, J.F. Content analysis of dam break studies for tailings dams with high damage potential in the Quadrilátero Ferrífero, Minas Gerais: Technical weaknesses and proposals for improvements. *Nat. Hazards* **2020**, *104*, 1141–1156. [CrossRef]
- 3. DWA (German Association for Water, Wastewater and Waste). *Bauwerksüberwachung an Talsperren*; DWA-Merkblätter, Nr. M 514; DWA: Hennef, Germany, 2011.
- 4. DIN 19700-10: 2004-07; Stauanlagen-Teil 11: Talsperren. Beuth Verlag GmbH: Berlin, Germany, 2004. [CrossRef]
- 5. Corsetti, M.; Fossati, F.; Manunta, M.; Marsella, M. Advanced SBAS-DInSAR technique for controlling large civil infrastructures: An application to the Genzano di Lucania dam. *Sensors* **2018**, *18*, 2371. [CrossRef]
- 6. Zinno, I.; Bonano, M.; Buonanno, S.; Casu, F.; De Luca, C.; Manunta, M.; Manzo, M.; Lanari, R. National scale surface deformation time series generation through advanced DInSAR processing of sentinel-1 data within a cloud computing environment. *IEEE Trans. Big Data* **2018**, *6*, 558–571. [CrossRef]
- 7. Bonì, R.; Bordoni, M.; Vivaldi, V.; Troisi, C.; Tararbra, M.; Lanteri, L.; Zucca, F.; Meisina, C. Assessment of the Sentinel-1 based ground motion data feasibility for large scale landslide monitoring. *Landslides* **2020**, *17*, 2287–2299. [CrossRef]
- 8. Duan, L.; Gong, H.; Chen, B.; Zhou, C.; Lei, K.; Gao, M.; Yu, H.; Cao, Q.; Cao, J. An improved multi-sensor MTI time-series fusion method to monitor the subsidence of Beijing subway network during the Past 15 Years. *Remote Sens.* **2020**, *12*, 2125. [CrossRef]
- 9. Crosetto, M.; Monserrat, O.; Iglesias, R.; Crippa, B. Persistent scatterer interferometry. *Photogramm. Eng. Remote Sens.* **2010**, 76, 1061–1069. [CrossRef]
- 10. Gernhardt, S.; Adam, N.; Eineder, M.; Bamler, R. Potential of very high resolution SAR for persistent scatterer interferometry in urban areas. *Ann. GIS* **2010**, *16*, 103–111. [CrossRef]
- 11. Crosetto, M.; Monserrat, O.; Cuevas-González, M.; Devanthéry, N.; Crippa, B. Persistent scatterer interferometry: A review. *ISPRS J. Photogramm. Remote Sens.* **2016**, *115*, 78–89. [CrossRef]
- 12. Lazecky, M.; Perissin, D.; Lei, L.; Qin, Y.; Scaioni, M. Plover Cove Dam Monitoring with Spaceborne InSAR Technique in Hong Kong. In Proceedings of the 2nd Joint International Symposium on Deformation Monitoring, Nottingham, UK, 9–10 September 2013; pp. 9–11. Available online: http://www.sarproz.com/wp-content/papercite-data/pdf/lazecky-pcdmwsitihk2013.pdf (accessed on 11 October 2024).
- 13. Milillo, P.; Porcu, M.C.; Lundgren, P.; Soccodato, F.; Salzer, J.; Fielding, E.; Bürgmann, R.; Milillo, G.; Perissin, D.; Biondi, F. The ongoing destabilization of the Mosul dam as observed by synthetic aperture radar interferometry. In Proceedings of the 2017 IEEE International Geoscience and Remote Sensing Symposium (IGARSS), Fort Worth, TX, USA, 23–28 July 2017; IEEE: Piscataway, NJ, USA, 2017; pp. 6279–6282. [CrossRef]
- Ruiz-Armenteros, A.M.; Lazecky, M.; Hlaváčová, I.; Bakoň, M.; Delgado, J.M.; Sousa, J.J.; Lamas-Fernández, F.; Marchamalo, M.; Caro-Cuenca, M.; Papco, J.; et al. Deformation monitoring of dam infrastructures via spaceborne MT-InSAR. The case of La Viñuela (Málaga, southern Spain). *Procedia Comput. Sci.* 2018, 138, 346–353. [CrossRef]
- 15. Marchamalo-Sacristán, M.; Ruiz-Armenteros, A.M.; Lamas-Fernández, F.; González-Rodrigo, B.; Martínez-Marín, R.; Delgado-Blasco, J.M.; Bakon, M.; Lazecky, M.; Perissin, D.; Papco, J.; et al. MT-InSAR and dam modeling for the comprehensive monitoring of an Earth-fill dam: The case of the Benínar dam (Almería, Spain). *Remote Sens.* 2023, 15, 2802. [CrossRef]
- 16. Abo, H.; Osawa, T.; Ge, P.; Takahashi, A.; Yamagishi, K. Deformation Monitoring of Large-Scale Rockfill Dam Applying Persistent Scatterer Interferometry (PSI) Using Sentinel-1 SAR Data. In Proceedings of the 2021 7th Asia-Pacific Conference on Synthetic Aperture Radar (APSAR), Virtual, 1–3 November 2021; IEEE: Piscataway, NJ, USA, 2021; pp. 1–6. [CrossRef]
- 17. Wang, Z.; Perissin, D. Cosmo SkyMed AO projects-3D reconstruction and stability monitoring of the Three Gorges Dam. In Proceedings of the 2012 IEEE International Geoscience and Remote Sensing Symposium, Munich, Germany, 22–27 July 2012; IEEE: Piscataway, NJ, USA, 2012; pp. 3831–3834. [CrossRef]
- 18. Milillo, P.; Perissin, D.; Salzer, J.T.; Lundgren, P.; Lacava, G.; Milillo, G.; Serio, C. Monitoring dam structural health from space: Insights from novel InSAR techniques and multi-parametric modeling applied to the Pertusillo dam Basilicata, Italy. *Int. J. Appl. Earth Obs. Geoinf.* 2016, 52, 221–229. [CrossRef]
- 19. Jänichen, J.; Schmullius, C.; Baade, J.; Last, K.; Bettzieche, V.; Dubois, C. Monitoring of Radial Deformations of a Gravity Dam Using Sentinel-1 Persistent Scatterer Interferometry. *Remote Sens.* **2022**, *14*, 1112. [CrossRef]
- 20. Grebby, S.; Sowter, A.; Gluyas, J.; Toll, D.; Gee, D.; Athab, A.; Girindran, R. Advanced analysis of satellite data reveals ground deformation precursors to the Brumadinho Tailings Dam collapse. *Commun. Earth Environ.* **2021**, *2*, 2. [CrossRef]
- Rana, N.M.; Delaney, K.B.; Evans, S.G.; Deane, E.; Small, A.; Adria, D.A.; McDougall, S.; Ghahramani, N.; Take, W.A. Application
 of Sentinel-1 InSAR to monitor tailings dams and predict geotechnical instability: Practical considerations based on case study
 insights. *Bull. Eng. Geol. Environ.* 2024, 83, 204. [CrossRef]
- 22. Bayik, C.; Abdikan, S.; Arıkan, M. Long term displacement observation of the Atatürk Dam, Turkey by multi-temporal InSAR analysis. *Acta Astronaut.* **2021**, *189*, 483–491. [CrossRef]

Remote Sens. 2025, 17, 2629 22 of 22

23. Schneider, P.; Soergel, U. Matching persistent scatterer clusters to building elements in mesh representation. *ISPRS Ann. Photogramm. Remote Sens. Spat. Inf. Sci.* **2022**, *3*, 123–130. [CrossRef]

- 24. Ruhrverband. So Funktioniert eine Talsperre. Bau- und Funktionsweise von Talsperren. 2025. Available online: https://ruhrverband.de/flussgebiet/talsperren/so-funktioniert-eine-talsperre (accessed on 7 February 2025).
- 25. Fleischer, H. Load-bearing behaviour of old dams and conclusions for structural monitoring. *Wasserwirtschaft* **2022**, *112*, 12–18. [CrossRef]
- 26. Ruhrverband. Glörtalsperre. Sicherheitsbericht. Teil A. Unpublished Security Report. 2021.
- 27. Ruhrverband. Glörtalsperre. Sicherheitsbericht. Teil B. Unpublished Security Report. 2021.
- 28. GDI-NRW. Geodateninfrastruktur Nordrhein-Westfalen. Geoportal NRW. 2021. Available online: https://www.gdi.nrw (accessed on 11 October 2024).
- 29. Bettzieche, V. Satellite monitoring of the deformations of dams. Wasserwirtschaft 2020, 110, 48–51. [CrossRef]
- 30. Delgado Blasco, J.M.; Ziemer, J.; Foumelis, M.; Dubois, C. SNAP2StaMPS v2: Increasing Features and Supported Sensors in the Open Source SNAP2StaMPS Processing Scheme. 2023. Available online: https://zenodo.org/record/8331352 (accessed on 11 October 2024).
- 31. Ziemer, J. TSX2StaMPS. 2022. Available online: https://github.com/jziemer1996/TSX2StaMPS (accessed on 7 February 2025).
- 32. Grassi, F.; Mancini, F. Sentinel-1 Data for Ground DEFORMATION monitoring: The SNAP-StaMPS Workflow. In Proceedings of the Workshop Tematico di Telerilevamento–Bologna, Bologna, Italy, 6 June 2019; Volume 26. Available online: https://www.researchgate.net/profile/Francesco-Mancini-4/publication/334163440_Sentinel-1_data_for_ground_deformation_monitoring_the_SNAP-StaMPS_workflow/links/5d25f878299bf1547ca94689/Sentinel-1-data-for-ground-deformation-monitoring-the-SNAP-StaMPS-workflow.pdf (accessed on 11 October 2024).
- 33. Ferretti, A.; Prati, C.; Rocca, F. Analysis of permanent scatterers in SAR interferometry. In Proceedings of the IGARSS 2000—IEEE 2000 International Geoscience and Remote Sensing Symposium, Taking the Pulse of the Planet: The Role of Remote Sensing in Managing the Environment, Proceedings (Cat. No. 00CH37120), Honolulu, HI, USA, 24–28 July 2000; IEEE: Piscataway, NJ, USA, 2000; Volume 2, pp. 761–763. [CrossRef]
- 34. Kalia, A.; Frei, M.; Lege, T. A Copernicus downstream-service for the nationwide monitoring of surface displacements in Germany. *Remote Sens. Environ.* **2017**, 202, 234–249. [CrossRef]
- 35. Ansar, A.M.H.; Din, A.H.M.; Latip, A.; Reba, M.N.M. A short review on Persistent Scatterer Interferometry techniques for surface deformation monitoring. *Int. Arch. Photogramm. Remote Sens. Spat. Inf. Sci.* **2022**, *46*, 23–31. [CrossRef]
- 36. Ziemer, J.; Jänichen, J.; Wicker, C.; Klöpper, D.; Last, K.; Kalia, A.; Lege, T.; Schmullius, C.; Dubois, C. Assessing the Feasibility of Persistent Scatterer Data for Operational Dam Monitoring in Germany: A Case Study. *Remote Sens.* 2025, 17, 1202. [CrossRef]
- 37. Haghighi, M.H.; Motagh, M. Sentinel-1 InSAR over Germany: Large-scale interferometry, atmospheric effects, and ground deformation mapping. *ZfV-Z. Geodasie Geoinf. Landmanagement* **2017**, 142, 245–256. [CrossRef]
- 38. Cleveland, W.S. Robust locally weighted regression and smoothing scatterplots. J. Am. Stat. Assoc. 1979, 74, 829–836. [CrossRef]
- 39. Lundberg, S.M.; Lee, S.I. A unified approach to interpreting model predictions. Adv. Neural Inf. Process. Syst. 2017, 30, 4768–4777.
- 40. Wittke, W.; Wittke, M.; Kiehl, J.R. Interaction of a masonry dam and the rock foundation. *Geotech. Geol. Eng.* **2012**, *30*, 581–601. [CrossRef]
- 41. Eshqi Molan, Y.; Lohman, R.; Pritchard, M. Ground displacements in ny using persistent scatterer interferometric synthetic aperture radar and comparison of x-and c-band data. *Remote Sens.* **2023**, *15*, 1815. [CrossRef]
- 42. Ferretti, A.; Monti-Guarnieri, A.; Prati, C.; Rocca, F.; Massonet, D. *InSAR Principles-Guidelines for SAR Interferometry Processing and Interpretation*; ESTEC: Noordwijk, The Netherlands, 2007; Volume 19. Available online: https://www.esa.int/esapub/tm/tm19/TM-19_ptA.pdf (accessed on 11 October 2024).
- 43. Cumming, I.; Zhang, J. Measuring the 3-D flow of the Lowell Glacier with InSAR. In Proceedings of the FRINGE '99: 2nd International Workshop on ERS SAR, Liege, Belgium, 10–12 November 1999.
- 44. Lazecky, M.; Hlavacova, I.; Bakon, M.; Sousa, J.J.; Perissin, D.; Patricio, G. Bridge displacements monitoring using space-borne X-band SAR interferometry. *IEEE J. Sel. Top. Appl. Earth Obs. Remote Sens.* **2016**, *10*, 205–210. [CrossRef]

Disclaimer/Publisher's Note: The statements, opinions and data contained in all publications are solely those of the individual author(s) and contributor(s) and not of MDPI and/or the editor(s). MDPI and/or the editor(s) disclaim responsibility for any injury to people or property resulting from any ideas, methods, instructions or products referred to in the content.